Deciphering phase stress partition and its correlation to mechanical anisotropy of laser powder bed fusion AlSi10Mg

Lubin Song[a], Shulin Yuan[a], Lv Zhao[a,c,*], Yaxin Zhu[a,c], Shuang Liang[a,c], Minsheng Huang[a,c], Aude Simar[b], Zhenhuan Li[a,c]

[a] *Department of Mechanics, School of Aerospace Engineering, Huazhong University of science and Technology, Wuhan, China*

[b] *Institute of Mechanics, Materials and Civil Engineering, UCLouvain, Louvain-la-Neuve, Belgium*

[c] *Hubei Key Laboratory of Engineering Structure Analysis and Safety Assessment, 1037 Luoyu Road, Wuhan, China*

Abstract

Laser powder bed fusion AlSi10Mg exhibits severe mechanical anisotropy, which hinders its applications in industrial field. In the present work, we investigated the mechanisms of anisotropy in the light of phase stress partition, using traditional crystal plasticity and mechanism-based strain gradient crystal plasticity models. Two representative volume elements of the Al-Si cellular structures, corresponding to 35℃ and 200℃ build platform temperatures, were built to assess the influences of Al matrix strength and strain gradient on phase stress partition and anisotropy. In addition, the maximum principal stress distribution of the Si-rich network was probed, based on which the potential damage sites and densities were evaluated. The results show that the anisotropic strength and damage both originate from the elongated Si-rich network. According to the comparison between the 35℃ and 200℃ materials, an increase in Al phase strength can change the phase stress partition and effectively mitigate

* Corresponding author. Department of Mechanics, School of Aerospace Engineering, Huazhong University of Science and Technology, Wuhan, China. E-mail address: lvzhao@hust.edu.cn (L. Zhao).

the anisotropy degree. Moreover, it is revealed that the strain gradient tends to alleviate anisotropy and delay damage evolution. The findings of this work can pave the way to developing high-performance LPBF Al alloys with lower degrees of anisotropy.

Keywords

Laser powder bed fusion; AlSi10Mg; Anisotropy; Crystal plasticity; Phase stress partition

1. Introduction

Additive manufacturing (AM) involves a layer-by-layer building strategy that allows to produce components with complex geometric shapes [1, 2]. Laser powder bed fusion (LPBF) plays a leading role in the field of metal additive manufacturing, and it is widely used in aerospace, automotive and biomedical fields [3-7]. Aluminum alloys made by LPBF are ideal candidates for complex and high-strength lightweight structures, while maintaining their traditional advantages, such as high strength-to-weight ratio, good corrosion resistance and low price. As a result, LPBF Al alloys have attracted extensive attentions and investigations, especially in the field of aerospace engineering [8-10].

LPBF AlSi10Mg is one of the most widely studied materials in the metal additive manufacturing field owing to its good printability and strength-to-weight ratio [11-14]. This alloy presents trans-scale, hierarchical and heterogeneous microstructure that is closely related to the high cooling rate (up to 10^6 K/s), strong thermal gradient (in the order of 10^6 K/m) and layer-wise scanning strategy of the LPBF process [7, 15, 16]. The microstructure of LPBF AlSi10Mg can be featured with nanoscale supersaturated solute atom clusters [17] and nano-particles [18], microscale Si-rich eutectic networks [19] and mesoscale melt pool (MP)

structure [20]. The Si-rich eutectic presents different morphologies and sizes in different MP zones [21, 22], namely, fine melt pool zone (FMP), coarse melt pool zone (CMP) and heat affected zone (HAZ), and it is much finer than that of cast AlSi10Mg.

Although LPBF imparts a higher strength to AlSi10Mg compared to their cast counterpart [19], the heterogeneous microstructure features induce a strong mechanical anisotropy, in terms of both strength and ductility, thus limiting the wide application of the material. Indeed, the yield strength and elongation to fracture along the building direction (i.e. vertical specimens) are mostly lower than those in the perpendicular direction (i.e. horizontal specimens), while the difference in tensile strength between the two directions is relatively smaller, as shown in Fig. 1. To drive further developments of LPBF Al alloys, the underlying mechanisms for the load direction dependent behaviors should be unraveled. Seeking the quantitative correlation between microstructure and mechanical properties is a remedy in this endeavor. According to nano-indentation tests, the melt pool border (i.e. CMP and HAZ, MPB in short) presents a lower strength than the melt pool interior (i.e. FMP) due to degraded Si-rich network [23, 24]. One may anticipate that the material strength is dictated by the MPB along the building direction, thus leading to a lower global yield strength compared to the horizontal direction. However, this viewpoint cannot explain the higher strain hardening ability along the building direction. Regarding the damage and fracture, some studies showed that the crack propagation was mostly along the melt pool border (MPB) and in the MP interior when the loading direction is parallel and perpendicular to the building direction, respectively [25-28]. This observation suggested that the lower ductility along the building direction could arise from premature

damage and crack along MPB. Nevertheless, Zhao et al. [29] and Yan et al. [30] showed that sound (i.e. incorporating a very low porosity of 0.13%) LPBF AlSi10Mg presented very similar ductility in different loading directions, although the lower-strength MPB was prone to strain localization and fracture when loaded along the building direction. Recently, Chen et al. [31] showed that the as built samples exhibited a strong mechanical anisotropy in both strength and ductility, whereas the anisotropy was significantly weakened for the post-heat treated counterparts incorporating the same crystal orientation distribution. From the abovementioned studies, it can be concluded that the anisotropic macro tensile properties are possibly not result of the heterogeneous MP structures or the crystal orientations.

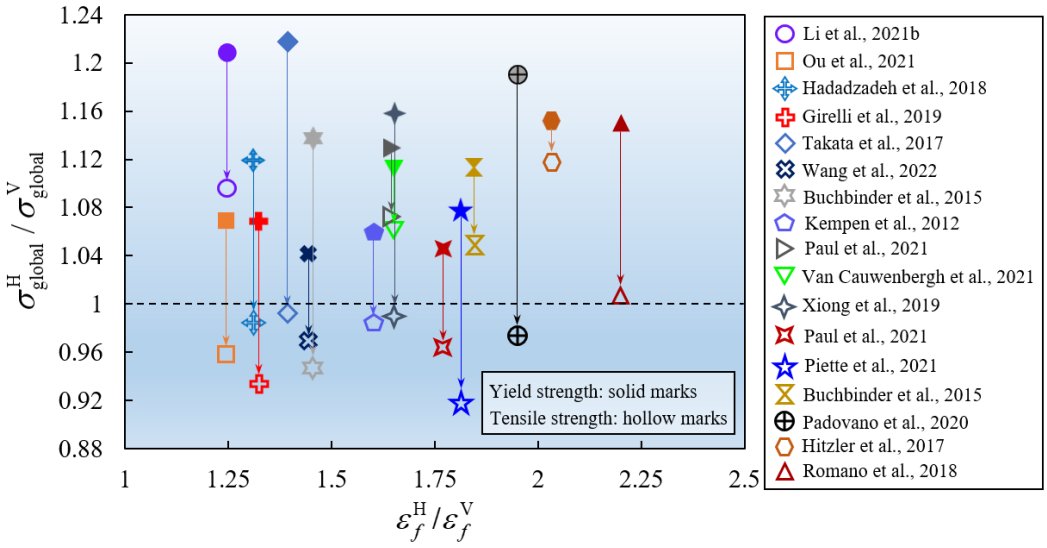

Fig. 1. Plot of literature data demonstrating the anisotropy of LPBF AlSi10Mg. The data are extracted from [11, 13, 26, 28, 32-42]. The superscripts H and V represent horizontal and vertical specimens, respectively.

Another key factor to anisotropy is related to the intrinsic anisotropic behavior of the Al-Si cellular structure, i.e. α-Al matrix and surrounding Si-rich network. Through high resolution focused ion beam/scanning electron microscopy (FIB/SEM) tomography, Santos Macías et al.

[19] have shown that the Si-rich eutectic network presents an elongated tubular shape toward the melt pool centerline, which is expected to exhibit a stronger load bearing capacity along the building direction [43]. Indeed, through micro-pillar compression tests, Li et al. [44] revealed a significant anisotropy of the FMP Al-Si cellular structure, the strength along the building direction being much higher. As LPBF AlSi10Mg is composed of relatively soft α-Al matrix and hard Si-rich eutectic, a modification of phase stress partition as a function of the loading direction could be responsible for the Al-Si cell anisotropy. Kim et al. [45] and Zhang et al. [46] investigated the evolution of phase stress using in situ tensile tests coupled with either neutron or X-ray diffraction, and it was found that the Si-rich eutectic exhibited a much higher internal phase stress than the α-Al matrix, hence contributing to a significant portion of global flow stress. However, no comparison between horizontal and vertical specimens was provided in these works. Furthermore, due to the limitation of measurement resolution, only averaged phase stresses could be assessed, which do not allow to study the behaviors of different melt pool zones. It is also noteworthy that the process parameters, such as the build platform temperature, can alter the cooling rate and thermal gradient during solidification [47, 48], therefore significantly changing the microstructure fineness and leading to large mechanical properties difference [19]. Performing advanced in situ experiments to investigate various microstructures is costly and tedious, alternative methods should be employed in this endeavor, for instance micromechanical simulations.

Micromechanical modeling and simulation can be powerful tools for building the link between microstructure and mechanical properties of LPBF metals [49-53], they also allow to

elucidate underlying mechanisms at the micro-scale which are difficult to access by experiments. Modeling and simulation works on LPBF AlSi10Mg are emerging in the literature, mostly based on phenomenological crystal plasticity constitutive models. Kim et al. [54] and Zhang and Andrä [43] analyzed the load partition and the contribution of the Al and Si phase stresses to macroscopic flow stress. However, in their studies, the Si-rich phase was simplified as particles with specific aspect ratio, and no comparison between different loading directions was provided. Jain et al. [55] simulated the stress-strain response using fast Fourier transform crystal plasticity model. Although the authors considered the cellular shape of the Al-Si cells, their model was quasi-2D (the dimension in the building direction is very low) and thus cannot be used to investigate the anisotropy issue. Li et al. [44] performed a systematic study addressing the anisotropic strength of the Al-Si cells revealed by micro-pillar compression tests, and they attributed the anisotropy to the elongated Al-Si cellular structure. However, the size and volume fraction of the Si-rich network were not accurately controlled in their model, which could affect the calculation and quantitative analysis of phase stress partition.

Analyzing the previous works, the following aspects should be further considered to drive a leap forward in the understanding of microstructure-performance correlation for LPBF AlSi10Mg:

(1) It is necessary to generate an experimentally-inspired realistic model for the Al-Si cellular structure to ensure accurate calculation of local phase stress distribution.

(2) It is not clear what other factors could significantly affect the anisotropy, for instance the strength of the α-Al matrix, given that different processing parameters may lead to different

microstructure features (i.e. solid solution and Si-rich nano-particles) within the α-Al matrix, thus imparting different levels of yield and tensile strengths.

(3) The influence of strain gradient (i.e. extra hardening of the α-Al matrix) on the phase stress partition was not considered in all previous works. Nevertheless, the harder Si phase would restrict the deformation of the softer Al near the interfaces, thus conferring a large strain gradient and consequently a high density of geometrically necessary dislocations (GNDs) near the Al/Si interfaces. Such phenomenon has been evidenced with transmission electron microscopy (TEM) by Li et al. [56], but its influence on anisotropy is unclear.

(4) None of previous works assessed the anisotropy in ductility. In fact, damage (i.e. microvoid) of LPBF AlSi10Mg has been shown to arise from fracture of brittle Si-rich network [18], the assessment of damage behavior can thus be associated with the stress level inside the brittle secondary phase [57].

The present paper aims to investigate the phase stress partition between the Al matrix and Si-rich network and its correlation to mechanical anisotropy of laser powder bed fusion AlSi10Mg. Two microstructures, obtained with two different building platform temperatures (i.e. 35℃ and 200℃) were considered, which, according to our previous experimental work [24], exhibit a weak and a strong anisotropy, respectively. Both phenomenological crystal plasticity (CP) and mechanism-based strain gradient crystal plasticity (MSG-CP) constitutive models were used to study the tensile behavior of the fine melt pool (FMP is the most representative microstructure of LPBF AlSi10Mg) along two loading directions. First, the representative volume elements (RVEs) of FMP Al-Si cellular structures were constructed, and

the anisotropic load bearing capacity of the elongated Si-rich network was analyzed. Second, the influence of the Al matrix strength on the phase stress partition was further assessed. Then, the effect of strain gradient on the flow stress and the phase stress partition was investigated. Finally, the potential damage sites and density (i.e. volume fraction of critical Si phase presenting high principal maximum stress) was analyzed, based on which the anisotropy in ductility was discussed.

2. Materials and modelling methodology

2.1 Materials preparation and microstructure characterization

The investigated LPBF AlSi10Mg samples were fabricated by an EOS M290 machine, equipped with a 252×252×25 mm EN AW 5083 aluminum alloy build platform. The powder used for the manufacturing presents a mean diameter of 28.5 μm. Two sets of plates of 5×35×150 mm were manufactured with the machine manufacturer suggested parameters (laser power = 390 W, layer thickness = 30 μm, hatch spacing = 0.19 mm, scanning speed =1300 mm/s, scan rotation = 67°) but different build platform temperatures, i.e. 35℃ and 200℃ [19]. The printed plates remained as built state for the following characterization.

The microstructure of the as built samples was characterized with scanning electron microscopy (SEM). Metallurgical polishing and chemical etching (using 0.5% HF solution) were applied to obtain appropriate phase contrast. The SEM observations were carried out with JSM-IT500A. SEM micrographs of the heterogeneous microstructure are shown in Fig. 2. The melt pool and the three distinct zones at the melt pool border are depicted in Fig. 2(a) and (b), respectively. It is noteworthy that the present work mainly addresses the influence of phase

stress partition between Si-rich network and α-Al matrix on anisotropy. As the FMP zone is the dominant constituent of the alloy (i.e. presents a significantly higher volume fraction compared to other zones), only the FMP Al-Si cellular structure was investigated. The Si-rich network morphologies in the FMP zone are shown in Fig. 2(c) and (d) for the build platform temperature of 35°C and 200°C, respectively. It can be seen that the 200°C Si-rich network presents larger diameter and wall thickness. A statistical analysis revealed that the diameters are 320±60 nm and 570±80 nm, the wall thicknesses are 50 nm and 70 nm, and the lengths are 1.66±0.36 µm and 1.74±0.39 µm for the 35°C and 200°C materials, respectively [19]. The definition of the dimensions is indicated in Fig. 2(e). Moreover, the Si-rich nano-particles embedded in the Al cells are much smaller in the 35°C material (see the inset of Fig. 2(c) and Fig. 2(d)).

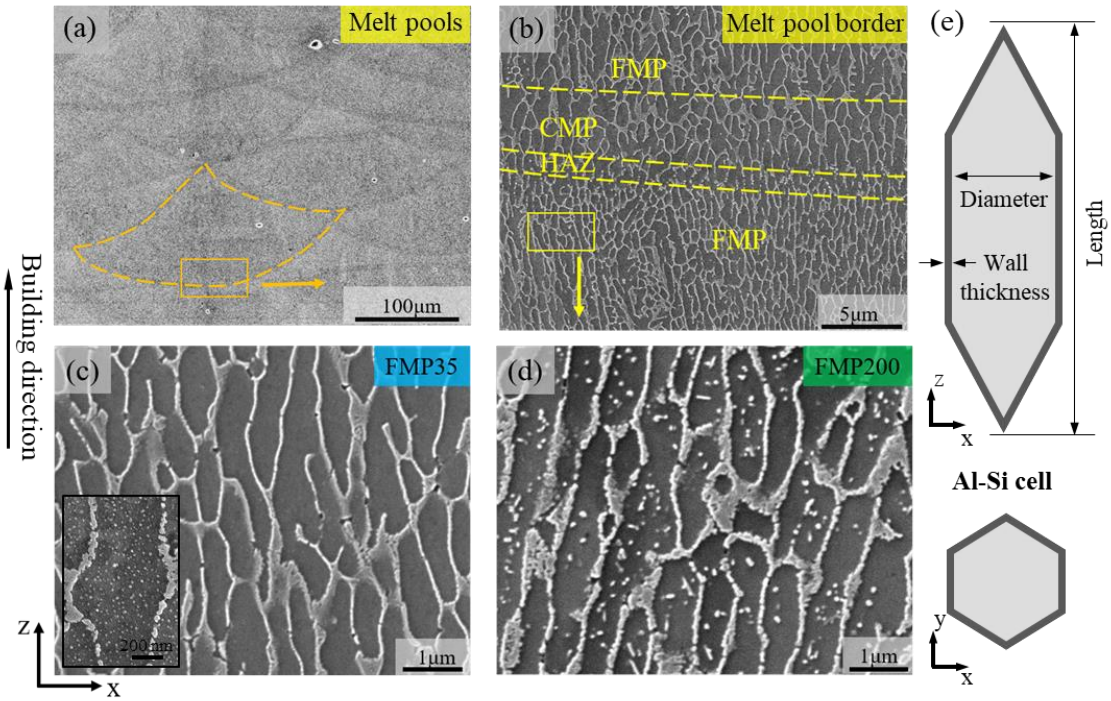

Fig. 2. Microstructure of the as built LPBF AlSi10Mg. SEM micrographs showing typical melt pool structures (a), three distinct zones near a melt pool border (b), Al cells and Si-rich networks in the FMP for

the 35°C (c) and 200°C (d) materials, respectively. Schematic drawing of the Al-Si cell morphology parallel and perpendicular to the building direction (e). The inset in (c) shows the nano-particles of the 35°C material.

To reveal the crystal orientation distribution, electron backscatter diffraction (EBSD) characterization was also performed (Zeiss supra 55VP) on both materials, more details can be found in a former work by Santos Macías et al. [19]. Fig. 3 shows the inverse pole figures for the two materials and the two loading directions. It can be seen that there exist a [100] texture along the building direction (vertical loading direction) and a slight [110] concentration along the perpendicular direction (horizontal loading direction). Therefore, the [100] and [110] crystal orientations were adopted when validating the RVE models with the experimental results.

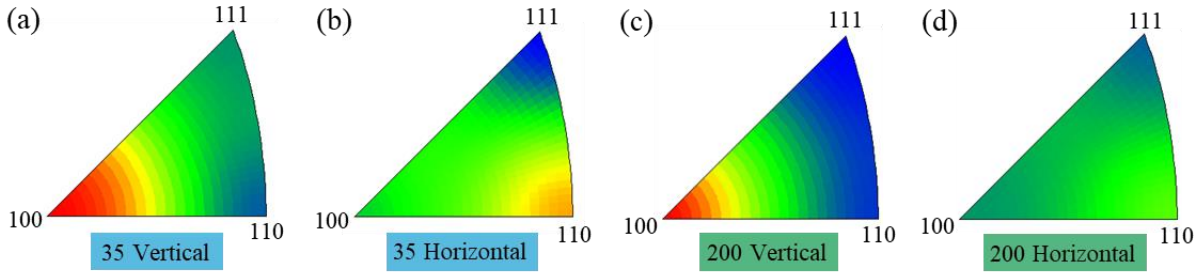

Fig. 3. Inverse pole figures showing the [100] texture along the vertical loading direction for the 35°C (a) and 200°C (c) materials, and the slightly preferred [110] crystal orientation along the horizontal loading direction for the 35°C (b) and 200°C (d) materials. The EBSD data provided in [19] were reused to plot these inverse pole figures

The results of tensile tests and damage characterization on the two materials have been published in our previous work [24], and they will be partly recalled in section 3.1 and 3.3 to compare with simulation results.

2.2 Crystal plasticity constitutive models

To investigate the effect of strain gradient on the phase stress partition, both the traditional crystal plasticity model [58] and the mechanism-based strain gradient crystal plasticity model (MSG-CP) [59] were used. These models were chosen due to their good ability to predict the plastic behavior of FCC metals and the simplicity for numerical implementation [60]. Following the continuum crystal plasticity framework proposed by Hill and Rice [61], Rice [62] and Asaro and Rice [63], the total plastic deformation gradient can be expressed by the standard multiplicative decomposition as:

$$\mathbf{F} = \mathbf{F}^{*}\mathbf{F}^{p} \tag{1}$$

where $\mathbf{F}^{*}$ is the elastic component, denoting the lattice stretching and rotation, and $\mathbf{F}^{p}$ is the plastic slip. The plastic velocity gradient $\mathbf{L}^{p}$ in the intermediate configuration can be described by:

$$\mathbf{L}^{p} = \dot{\mathbf{F}}^{p}\mathbf{F}^{p-1} = \sum_{\alpha} \dot{\gamma}^{(\alpha)} \boldsymbol{s}_0^{(\alpha)} \otimes \boldsymbol{m}_0^{(\alpha)} \tag{2}$$

where $\dot{\gamma}^{(\alpha)}$ is the slip rate of the slip system α. $\boldsymbol{s}_0^{(\alpha)}$ and $\boldsymbol{m}_0^{(\alpha)}$ are the slip direction vector and slip place normal vector in the reference configuration, respectively. The slip rate $\dot{\gamma}^{(\alpha)}$ can be related to the stress acting on the slip system α by:

$$\dot{\gamma}^{(\alpha)} = \dot{\gamma}_0 \left| \frac{\tau^{(\alpha)}}{g^{(\alpha)}} \right|^{n} \operatorname{sign}(\tau^{(\alpha)}) \tag{3}$$

where $\dot{\gamma}_0$ is the reference strain rate, $g^{(\alpha)}$ is the current slip strength of the slip system α, n is the strain sensitivity exponent, $\tau^{(\alpha)}$ is the resolved shear stress.

The rate of current slip strength $\dot{g}^{(\alpha)}$, i.e. the strain hardening rate, can be expressed with the evolution of slip rate as:

$$\dot{g}^{(\alpha)} = \sum_{\beta} h_{\alpha\beta} \dot{\gamma}^{(\beta)} \tag{4}$$

where $h_{\alpha\beta}$ denotes the slip hardening moduli, $h_{\alpha\alpha}$ $(\alpha = \beta)$ and $h_{\alpha\beta}$ $(\alpha \neq \beta)$ are self-hardening and latent hardening moduli, respectively, which read:

$$h_{\alpha\alpha} = h(\gamma) = h_0 \sec h^2 \left| \frac{h_0 \gamma}{\tau_s - \tau_0} \right| \quad (\alpha = \beta) \tag{5}$$

$$h_{\alpha\beta} = q h(\gamma) \quad (\alpha \neq \beta) \tag{6}$$

where h_0 is the initial hardening modulus, τ_0 the initial yield stress, τ_s the saturation flow stress, q a constant (q=1.0 for isotropic hardening), and γ the accumulated plastic shear strain:

$$\gamma = \sum_{\alpha} \int_0^t \left| \dot{\gamma}^{(\alpha)} \right| dt \tag{7}$$

The main difference between the aforementioned CP model and the MSG-CP model proposed by Han et al. [59] lies in the current slip resistance. The enhancement of the effective slip resistance $g_T^{(\alpha)}$ by strain gradient can be expressed by the Taylor hardening relation [64]:

$$g_T^{(\alpha)} = g_0 \sqrt{(g^{(\alpha)} / g_0)^2 + l \eta_G^{(\alpha)}} \tag{8}$$

where g_0 denotes the reference slip resistance (typically $\mu / g_0 \approx 100$), η_G^{α} the effective strain gradient and l the intrinsic material length defined as:

$$l = \frac{a^2 \mu^2 b}{(g_0)^2} \tag{9}$$

where a denotes the empirical coefficient (varies in the range of 0.2-0.5), μ the shear modulus, b the magnitude of the Burgers vector.

Therefore, the plastic shear rate on slip system α can be modified as:

$$\dot{\gamma}^{(\alpha)} = \dot{\gamma}_0 \left| \frac{\tau^{(\alpha)}}{g_T^{(\alpha)}} \right|^n \operatorname{sign}(\tau^{(\alpha)}) \tag{10}$$

The afore-presented constitutive models have been implemented with the Abaqus user-material (UMAT) subroutine based on the work by Huang [58]. Two sets of model parameters were used for the 35℃ and 200℃ materials in present work, as presented in Table 1. The Si-rich eutectic network was considered to be elastoplastic, as some plasticity signs (i.e. shear steps) were observed by TEM [54]. The parameters identified by Li et al. [44] were adopted for the 200℃ material, given the similar macroscopic tensile curves. Regarding the 35℃ material, the same parameters as the 200℃ material were assigned to the Si phase, while the parameters τ_0, τ_s and h_0 for the Al matrix were much larger than those of the 200℃ material, due to the much finer Si nano-particles imparting a higher strength. Following preliminary calculations, these parameters were fixed such that the relative differences of the yield strength and tensile strength between the 35℃ and 200℃ materials obtained by the simulations were close to that revealed by the tensile tests [19], see section 3.1. Specifically, the additional parameters for the MSG-CP model a=0.3, μ=27 GPa and b=0.286 nm for the Al matrix were extracted from the literature [65-67].

Table 1. Crystal plasticity model parameters for the Al and Si phases of LPBF AlSi10Mg

Parameter	Phase Al (35℃)	Phase Al (200℃)	Phase Si
τ_0 (MPa)	120.0	85.0	500.0

τ_s (MPa)	185.0	100.0	800.0
h_0 (MPa)	500.0	320.0	5000.0
$\dot{\gamma}_0$ (s^{-1})	0.001	0.001	0.001
m	35.0	35.0	35.0
C_{11} (GPa)	107.3	107.3	166.2
C_{12} (GPa)	60.9	60.9	64.4
C_{44} (GPa)	23.8	23.8	79.7
a	0.3	0.3	-
μ (GPa)	27.0	27.0	-
b (nm)	0.286	0.286	-

2.3 Geometrical models and simulations

2.3.1 Generation of the representative volume element

The representative volume elements (RVEs) of the Al-Si cellular structure were constructed based on a step-by-step (SSP) packing method proposed by Romanova and Balokhonov [68]. Additional steps were included to generate the Si-rich networks and to ensure the geometry periodicity. It is noteworthy that the Si nano-particles inside the Al matrix were not modeled in the geometrical model, but their strengthening effect for the Al phase was considered in the parameters. The main steps for the model generation is shown in Fig. 4 and summarized as follows:

- The model construction begins with discretizing a cuboid using a regular hexahedral mesh. Each element was initially assigned with a digital index that is equal to zero (DIe = 0). Then, a certain amount of seeds were semi randomly generated according to the Al-Si cell numbers N and assigned with DIs=1:N. The term “semi randomly” should be understood as follows: the x and y coordinates of the seeds were randomly selected in the entire

definition domain, whereas the z coordinate was forced to be random within two ranges of the domain height (here, [2/10*h, 3/10*h] and [7/10*h, 8/10*h]) to generate roughly two layers of seeds (see the snapshot of seed growth in Fig. 4) along the building direction (z axis). Such treatment will ensure the elongated shape of the Si-rich network.

- The seeds were then reduplicated and arranged periodically. Note that the reduplicated seeds presented the same DIs as their parent seeds. Afterwards, an ellipsoid growth algorithm was used to drive the growth of all seeds (i.e. original and reduplicated), during which the DIe of each element was replaced by the DIe of the growing seed embedding the element. This process ended until all DIe became nonzero.
- Subsequently, the elements with the same DIe were grouped into a same Al-Si cell (no Si-rich network was created at this stage), and Al cells without Si-rich network were generated. Then, the elements on the boundaries between neighboring Al cells were identified as the Si-rich networks. The numbers of elements on the boundaries could be adjusted to fit to the thickness of the Si-rich network.
- Afterwards, the elements belonging to the Al matrix and the Si-rich networks were separated into two sets, which allowed to assign the corresponding material properties. Finally, an Abaqus input file was created, to which the information for the nodes, elements and element sets was imported.

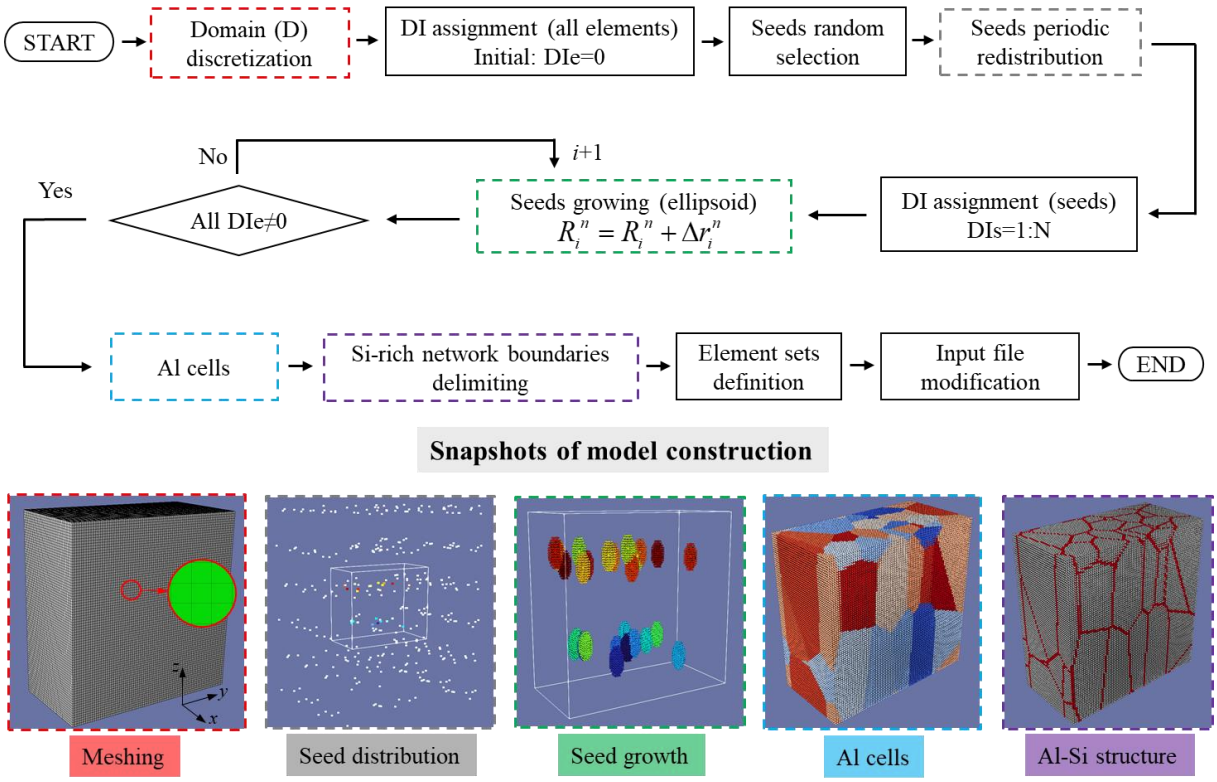

Fig. 4. The main steps for the generation of FMP representative volume element.

The length, width and height of the RVEs are 4 μm, 2 μm and 4 μm, respectively. Two models with different diameters and wall thicknesses of the Si-rich network were built, namely FMP 35 and FMP 200 (for the 35℃ and 200℃ materials, respectively), as shown in Fig. 5. This is achieved by assigning different seed numbers (i.e. 36 and 15 for the FMP 35 and FMP 200 models, respectively). The FMP 35 model incorporates a Si-rich network diameter of 0.6 ±0.15 μm, length of 2±0.25 μm and wall thickness of 50 nm, while the three parameters are 1 ±0.3 μm, 2±0.6 μm and 100 nm for the FMP 200 model. Although these dimensions present some deviations from the experimental measurement, the volume fraction of the Si-rich network was controlled to 13.8% for both models, which is obtained from the FIB/SEM tomography data [19]. Moreover, the ratios of the Si network diameter and length between FMP35 and FMP200 are close to that of the experimental characterization (roughly 0.56 and

1.05, respectively). Therefore, the two models can be used to evaluate the anisotropic behavior of the 35℃ and 200℃ materials and compare their difference. Periodic boundary conditions in all three directions were imposed on the RVEs. Two loading directions (i.e. vertical and horizontal), along which an engineering tensile strain of 0.1 was prescribed, were applied to investigate the anisotropic behavior of the Al-Si cellular structure. It should be noted that the Al matrix in the Al-Si cellular model is a single crystal. The [100] and [110] orientations were assigned, in consistence with the grain orientation distribution (see Fig. 3).

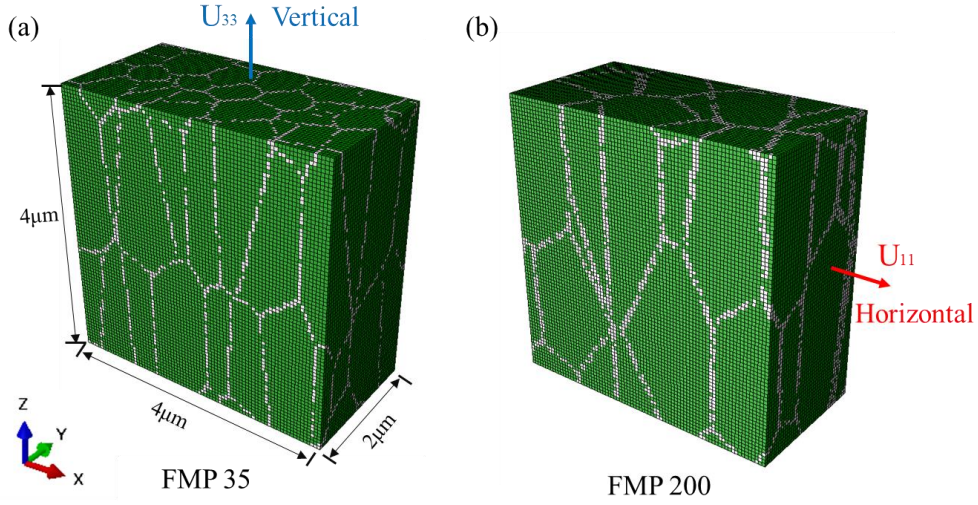

Fig. 5. Representative volume elements of FMP 35 (a) and FMP 200 (b). The vertical and horizontal loading directions are parallel and perpendicular to the building direction, respectively.

2.3.2 Model validation

The element type used for the calculations was C3D8 with full integration. To verify the convergence of the simulation results, five FMP 35 models were created, containing 108000, 171500, 256000, 364500 and 500000 elements, respectively. The engineering stress-strain curves are shown in Fig. S1(a) of the supplementary material. It is found that the simulation results converge when the element number exceeds 200000. Finally, the model with 256000

elements (element size of 50 nm) was chosen for both the FMP 35 and FMP 200 models. To verify the independence of the simulation results on the runs of model construction, three models with different semi-random seed distributions were created. The engineering stress-strain curves are shown in Fig. S1(b) of the supplementary material. The results are very close to each other, demonstrating that our model construction strategy is reasonable and the seed number is sufficient.

3. Results and discussion

In order to investigate the load partition between the Al matrix and the Si-rich network, the average phase stress in each phase was calculated by:

$$\sigma_{\text{ave}}^{(j)} = \sum_{i=1}^{N_{\text{p}}} \sigma_i^{(j)} \Omega_i \Big/ \sum_{i=1}^{N_{\text{p}}} \Omega_i \tag{11}$$

where $\sigma_i^{(j)}$ is the stress component along the loading direction (j) at the integration point i, Ω_i is the corresponding volume of the integration point and N_{p} is the total number of the integration points. The engineering strain in all figures hereinafter refers to the global deformation of the RVE in the corresponding loading direction.

In this section, the simulation results will be presented and discussed based on three aspects. First, the validity of the model parameters is verified, and the influence of Al matrix strength on strength anisotropy is assessed in section 3.1. Subsequently, the effect of strain gradient on flow strength and anisotropy is analyzed in section 3.2. Finally, the potential damage sites and distributions are discussed and related to anisotropy in ductility in section 3.3.

3.1 Influence of Al matrix strength on phase stress partition and anisotropy

The crystal plasticity model without strain gradient effect is used to validate the parameters for the two microstructures. Herein, the [100] and [110] orientations are used for the vertical and horizontal loading directions, respectively, in accordance with the measured grain orientation distribution (see Fig. 3). The experimental tensile curves extracted from our previous work [24] are replotted in Fig. 6(a) and the simulation results are presented in Fig. 6(b). It can be seen that the selected parameters can effectively reflect the weak and strong strength anisotropies of the 35°C and 200°C materials, respectively. Moreover, the relative differences in strength between the 35°C and 200°C materials obtained by the simulations are close to that revealed by the tensile tests, roughly 40% for the yield strength and 50% for the flow stress at the strain of 0.1.

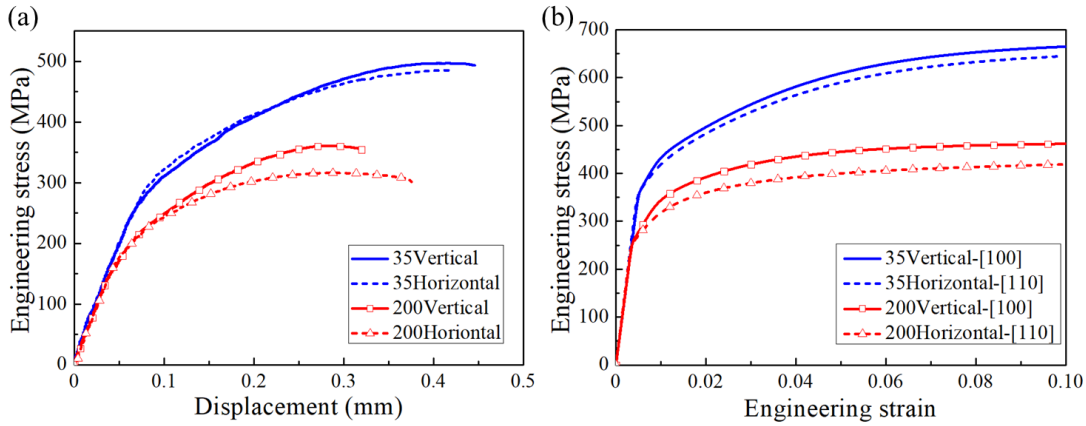

Fig. 6. Comparison of engineering stress-strain curves between the experiment results (a) and the crystal plasticity simulations (b). The experimental tensile curves are extracted from our previous work [24].

The comparison between Fig. 6(a) and (b) should be considered qualitative, which serves to verify the validity of the model parameters for the 35°C material. Quantitatively, the simulations with the periodic Al-Si cellular model provide higher flow stresses compared to the tensile experiments, as also reported in [44], from which the parameters for the 200°C

material have been extracted. This deviation can be explained by three factors: first, the elongated Al-Si cells are modeled to be aligned with the building direction (see Fig. 7(b)), whereas they change orientations when deviating from the centerline of the melt pool in real microstructure (see Fig. 7(a)); second, the RVE model does not incorporate the CMP and HAZ which could lower the macroscopic strength; third, the mean Schmidt factor is around 0.45 for the two materials along the two loading directions [24], while the [100] and [110] orientations assigned to the model exhibit a smaller Schmidt factor of 0.408. Although the simulation results with the Al-Si cellular model are not quantitatively identical to the tensile curves, they exhibit the same trend: the 35°C material exhibits a higher strength but a lower anisotropy compared to the 200°C counterpart. Therefore, the simulations with the Al-Si cellular models and the parameters listed in Table 1 can be used to assess the mechanism of mechanical anisotropy as well as the influencing factors, which is the core of the present work.

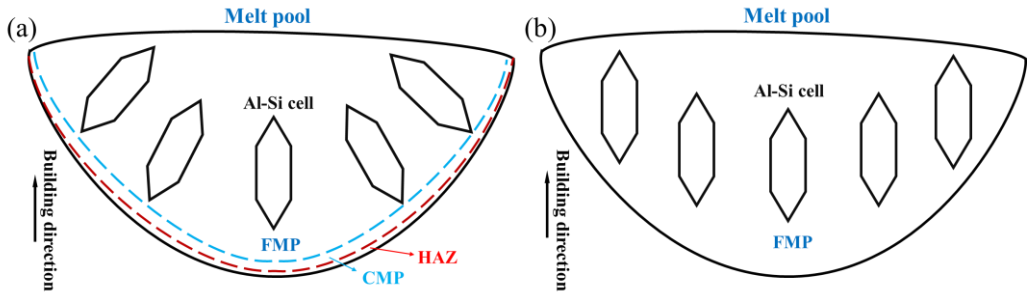

Fig. 7. Schematic drawings for the realistic microstructure of a melt pool (a) and the simplified microstructure for the simulations at the Al-Si hierarchy (b).

The strength anisotropy has been proposed to arise from the elongated Si-rich network [44], which exhibits a higher load bearing capacity along the vertical loading direction. But, why is anisotropy much stronger for the 200°C material, given that the 35°C counterpart also

presents elongated Al-Si cells (see Fig. 2c)? To understand the origin of that difference, the influence of the Al matrix strength on the anisotropy is analyzed, as the Al matrix is much softer in the 200°C material [19]. Herein, the crystal orientation is set to [110] for all the simulations to decouple the effect of the crystal orientation on the results. The stress-strain curves and the corresponding stress ratios between the vertical and horizontal directions (i.e. $\sigma^{V}_{global} / \sigma^{H}_{global}$) are presented in Fig. 8(a) and (b), showing again the relatively weak and strong degrees of anisotropy for the FMP 35 and FMP 200 models, respectively. Moreover, the evolutions of the averaged phase stresses along the two loading directions (i.e. horizontal and vertical) are calculated and presented in Fig. 8(c) and (d) for the Al matrix and Si-rich network, respectively. It can be seen, for both materials, that the internal stress of the Al matrix is almost insensitive to the loading direction, whereas the Si phase presents a significantly larger internal stress along the vertical direction, in accordance its higher load bearing capacity in this direction. Interestingly, the difference in Si phase stress between the two loading directions becomes weaker when the Al matrix is stronger (i.e. for the FMP 35), as can be seen in Fig. 8(d). In other words, the phase stress partition along the two loading directions can be significantly affected by the intrinsic strength of the Al matrix.

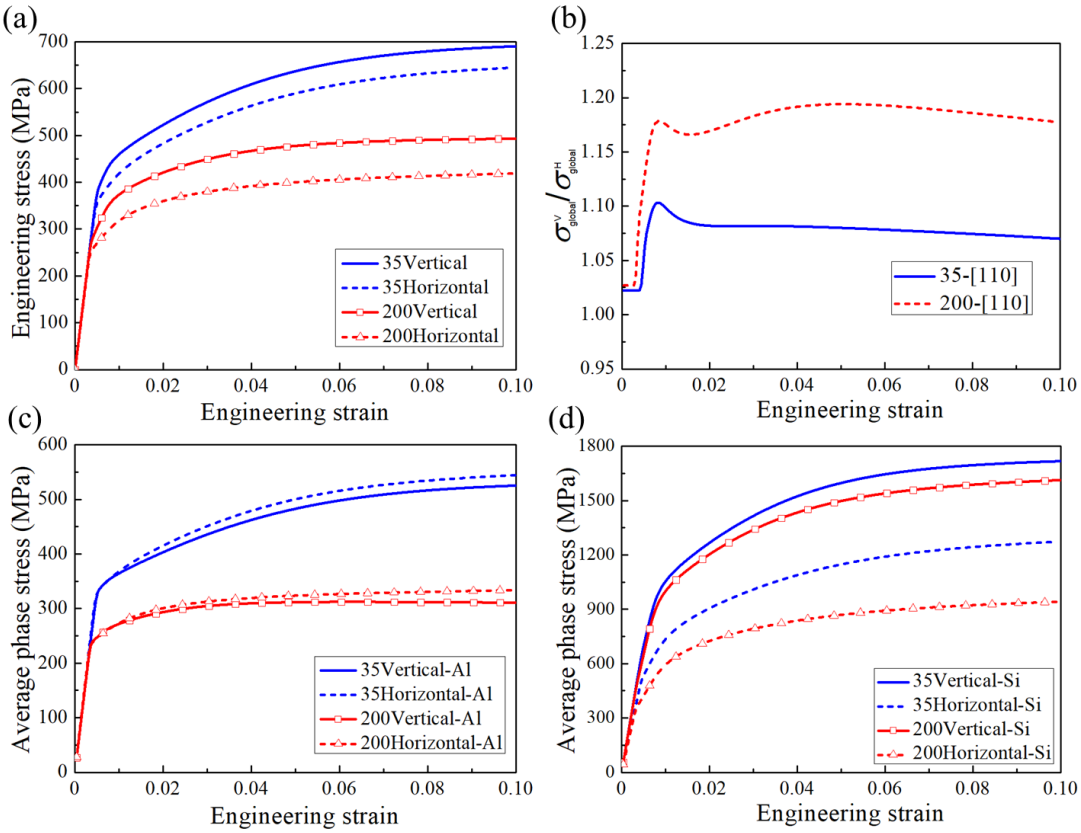

Fig. 8. Comparison of stress-strain curves (a) and global flow stress ratios between the vertical and horizontal directions (b) for the FMP 35 and FMP 200 models, evolutions of the average phase stresses for the Al (c) and Si phases (d). The crystal orientation is [110] for all the simulations.

To more clearly demonstrate the impact of the Al phase strength on the phase stress partition, the average phase stress ratios along the two loading directions (i.e. $\sigma^{V}_{phase} / \sigma^{H}_{phase}$) and the phase stress partition analysis are presented in Fig. 9(a) and (b), respectively. Fig. 9(a) shows that the stress ratio of the Al phase is close to 1.0 for both the FMP 35 and FMP 200. In contrast, the stress ratio of the Si phase is larger than 1.0 and significantly changes with the Al matrix strength. In the strain hardening stage, this ratio converges to 1.7 and 1.3 for the FMP 200 and FMP 35 models, respectively. This means that when the Al matrix presents a relatively low strength (i.e. the 200°C material), the Si-rich network exhibits a much higher load bearing

capacity in the vertical direction, thus leading to a larger stress contribution to the global flow stress (see Fig. 9(b)) and a marked anisotropy. On the other hand, when the Al matrix is strong (i.e. the 35℃ material), the gap in Si phase stress partition between the two loading directions is reduced (see Fig. 9(b)), and consequently the global flow stress presents a weaker anisotropy. One may anticipate naturally that if the Al matrix and Si-rich network presented the same strength, the anisotropy would totally vanish.

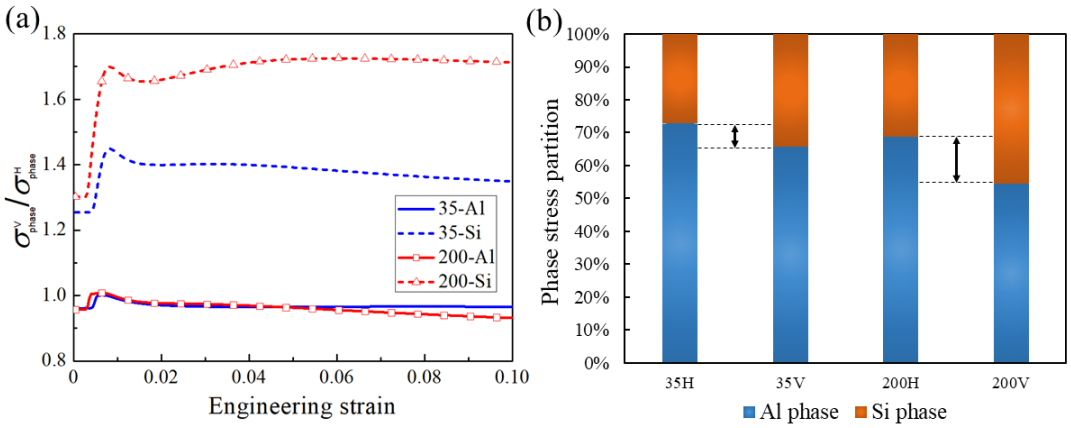

Fig. 9. Average phase stress ratios along the two loading directions (a) and the phase stress partition at the strain of 0.1 (b) for the FMP 35 and FMP 200 models presenting both a [110] orientation.

In summary, the results in this section show that the elongated Si-rich network is one of the main reasons for the strength anisotropy of LPBF AlSi10Mg. Nevertheless, the strength of the Al matrix strongly affects the phase stress partition and the global flow strength under different loading directions. To mitigate the strength anisotropy, one potential solution is to increase the strength of the Al matrix via for example smaller and denser nano-particles inside the Al cell.

3.2 Effect of strain gradient on flow stress and phase stress partition

The plastic deformation behaviors of metals are closely related to dislocations. Regarding LPBF AlSi10Mg, the hard Si-rich network constraints the deformation of the soft Al matrix, thus generating strain gradient (i.e. geometrically necessary dislocations, GNDs) at the vicinity of the Al-Si interface during plastic deformation [56]. In order to analyze the influence of strain gradient on the phase stress partition and strength anisotropy of LPBF AlSi10Mg, both CP and MSG-CP simulation results are presented and compared in this section. Here again, to decouple the effect of the crystal orientation on the results, the crystal orientation is set to [110] for all simulations. It should also be noted that only the strain gradient effect for the Al phase is considered in the present work.

The engineering stress-strain curves for the FMP 35 and FMP 200 models are shown in Fig. 10(a) and (b), respectively. It is found that the strain gradient improves the hardening ability in both loading directions, especially for the FMP 200 model (i.e. relatively softer Al matrix). This is particularly visible for an engineering strain larger than 0.05 for the FMP 35 model (Fig. 10 (a)) and 0.03 for the FMP 200 model (Fig. 10 (b)). To further analyze the origin of the increase in global flow stress, the phase stress evolutions are presented in Fig. 10(c) and (d) for the Al and Si phases, respectively. Concerning the Al matrix (Fig. 10 (c)), the internal phase stress is enhanced by the strain gradient for both materials and both loading directions, as more clearly reflected by the stress distribution contours shown in Fig. 11. Moreover, the magnitude of the Al phase stress increase is higher for the FMP 200 model compared to the FMP 35 counterpart (see also Fig. 11). For the Si-rich network (Fig. 10(d)), the strain gradient induced phase stress increase is almost negligible for the FMP 35, while it becomes much more

significant for the FMP 200. The aforementioned observations can be explained by the following. On the one hand, the Al matrix of the FMP 200 model is softer than that of the FMP 35 model, the plastic strain gradient at the Al-Si interface is therefore stronger in the FMP 200 model, leading to a more significant strain hardening of Al matrix compared to the FMP 35 (see also Fig. 11). On the other hand, when the internal stress of the Al matrix is effectively enhanced by the strain gradient, the Si phase stress will also be increased due to the load transfer between the two phases.

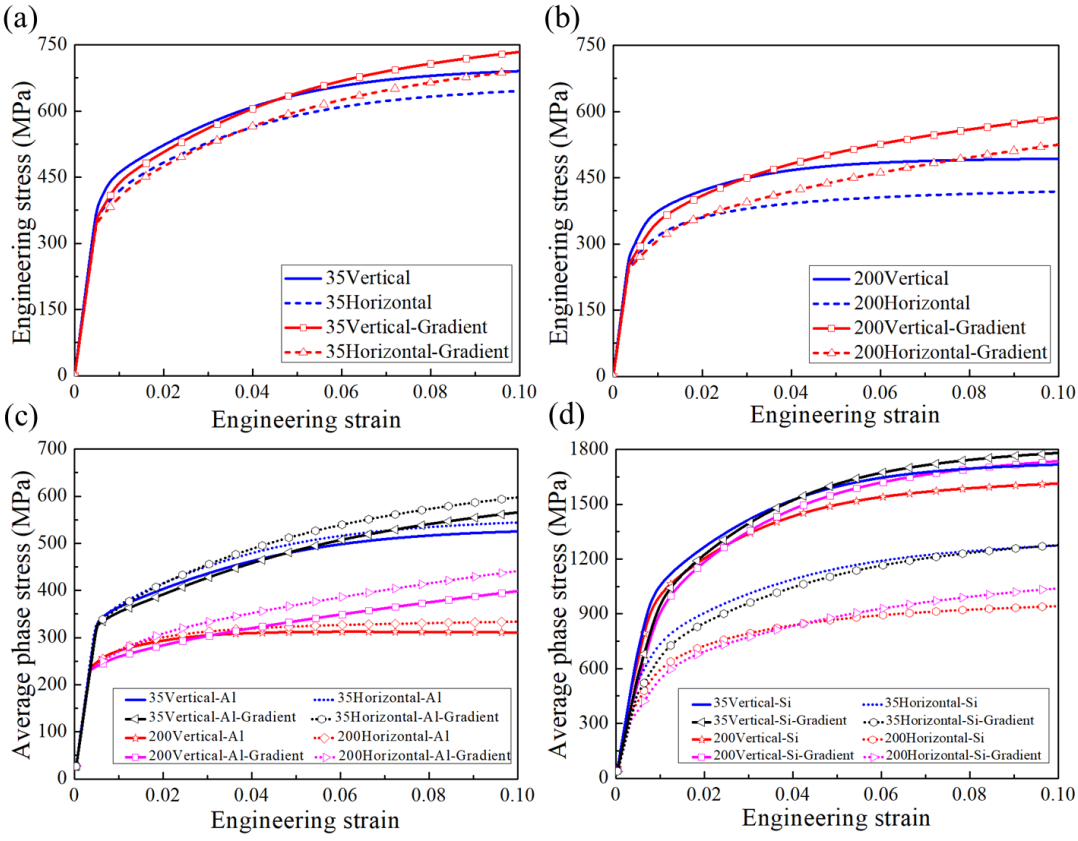

Fig. 10. Comparison of stress-strain curves with and without strain gradient for the FMP 35 (a) and FMP 200 (b) models, comparison of average phase stress evolutions with and without strain gradient for the Al (c) and Si (d) phases.

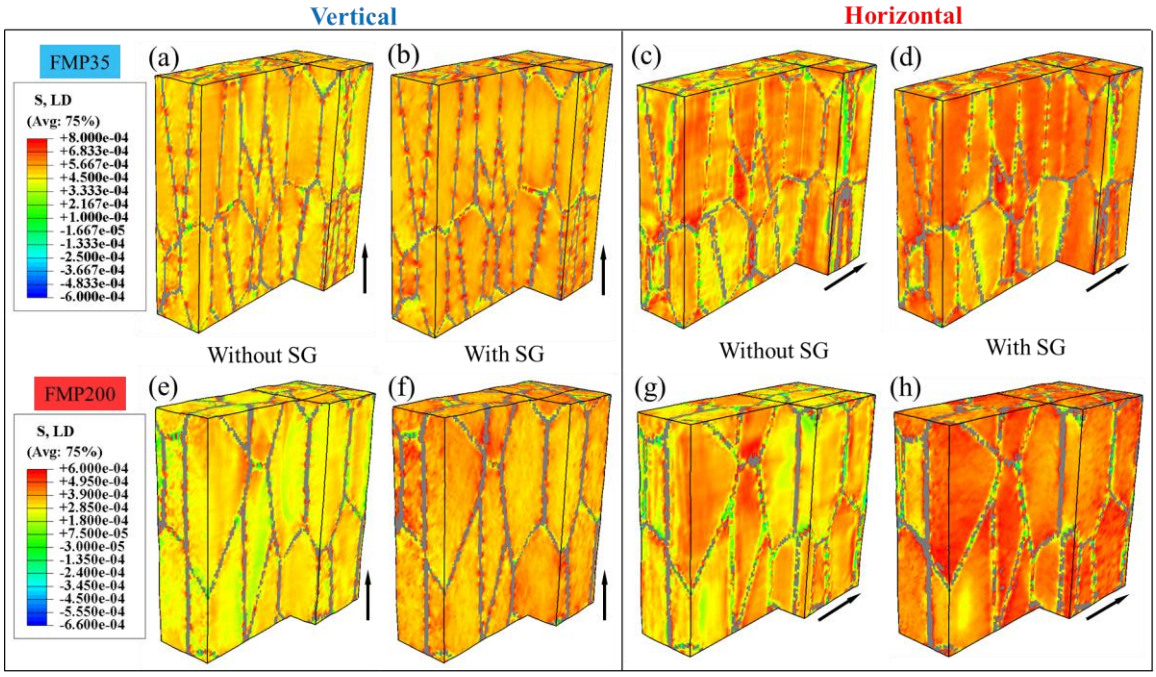

Fig. 11. Stress contours along the loading direction (LD, also indicated by the arrows). The FMP 35 model without (a) and with strain gradient (b) along the vertical direction, the FMP 35 model without (c) and with strain gradient (d) along the horizontal direction, the FMP 200 model without (e) and with strain gradient (f) along the vertical direction, the FMP 200 model without (g) and with strain gradient (h) along the horizontal direction. The stress unit is 10^6 MPa. The region in gray color represents the Si-rich network.

As for the anisotropy, Fig. 12(a) shows that the strain gradient tends to weaken the difference in flow stress between the two loading directions, the effect being more significant for the FMP 200 model. The previous paragraph has shown that the strain gradient increases the effective flow stress of the Al matrix (see Fig. 10(c)). Therefore, a harder Al phase weakens the strength anisotropy, similarly to the conclusion of section 3.1. Nevertheless, the underlying mechanism is bit different. In section 3.1, the higher (lower) anisotropy degree is mainly induced by the higher (lower) Si phase stress ratio between the two loading directions (see Fig. 9(a)). When comparing the phase stress ratios for the cases with and without strain gradient

effect (see Fig. 12(b)), it is found that the decrease of anisotropy is not associated with the decrease of Si phase stress ratio, the latter remains the same or even slightly increases. In fact, the decrease of anisotropy is associated with the Al phase stress ratio. Indeed, the Al phase stress ratio ($\sigma_{Al}^{V}/\sigma_{Al}^{H}$) is generally smaller than 1.0 (see Fig. 9(a)) since the Si-rich network induced constraint is more severe in the horizontal direction. This ratio is further reduced by the strain gradient effect (see Fig. 12(b)), partially compensating the difference of the global flow stresses between the two loading directions resulting from the Si phase stress ratio much higher than 1.0.

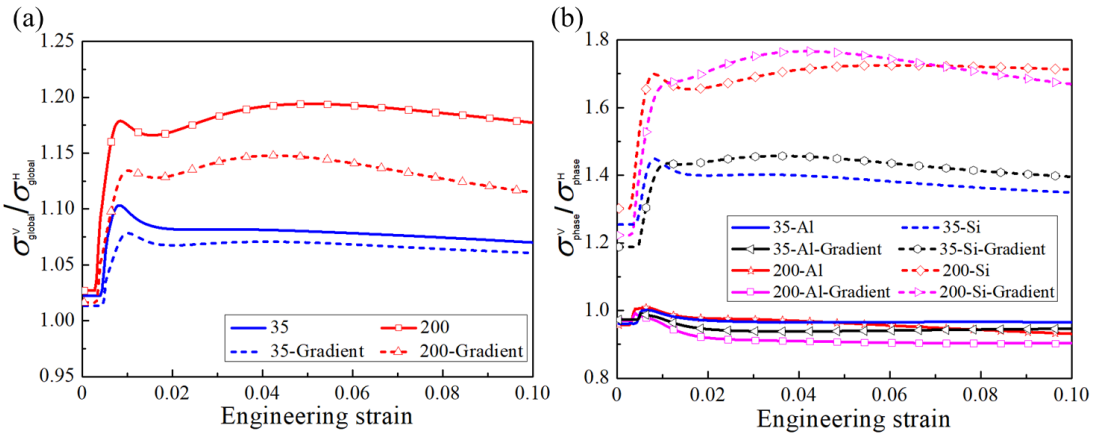

Fig. 12. Influence of strain gradient on the global flow stress ratios (a) and average phase stress ratios (b) between the two loading directions.

In summary, it has been revealed in this section that accounting for strain gradient effect in the CP model effectively increases the overall flow stress of the material and weakens anisotropy. In the following section, it will be shown that strain gradients significantly alter the stress distribution of the Si-rich network, thus potentially impacting the damage behavior. Therefore, when identifying model parameters with experimental data, the effect of strain

gradient cannot be set aside in future studies, especially when treating a case of intrinsically soft Al matrix.

3.3 Correlation between potential damage sites and ductility anisotropy

It has been shown in previous literature that the damage of LPBF AlSi10Mg arises from the fracture of the Si-rich network [18, 19, 69]. In this sense, the most probable damage sites can be assessed with the maximum principal stress distribution within the Si-rich network. The focus is set in this section on the analysis of potential damage density and its correlation to anisotropy in ductility. The results obtained with both the CP and MSG-CP models (for the [110] orientation) are shown and compared to investigate the influence of strain gradient on the damage behavior.

Fig. 13 shows the damage distribution in the FMP of the 35°C and 200°C materials under the horizontal and vertical loading directions. The observation areas are at the mid-thickness plane and close to the fracture surface, as schematically illustrated in the inset of Fig. 13. Fig. 13(b) and (d) show that the damage density is quite low for the horizontal direction. Regarding the vertical direction, the damage density is also low for the 35°C material (although a bit higher than the horizontal direction) but quite high for the 200°C material (see Fig. 13(a) and (c)). According to our previous work [24], the damage initiates very late for the FMP35-Horizontal, FMP35-Vertical and FMP200-Horizontal cases, while much earlier in the FMP200-Vertical case. This explains the difference in damage density observed in Fig. 13.

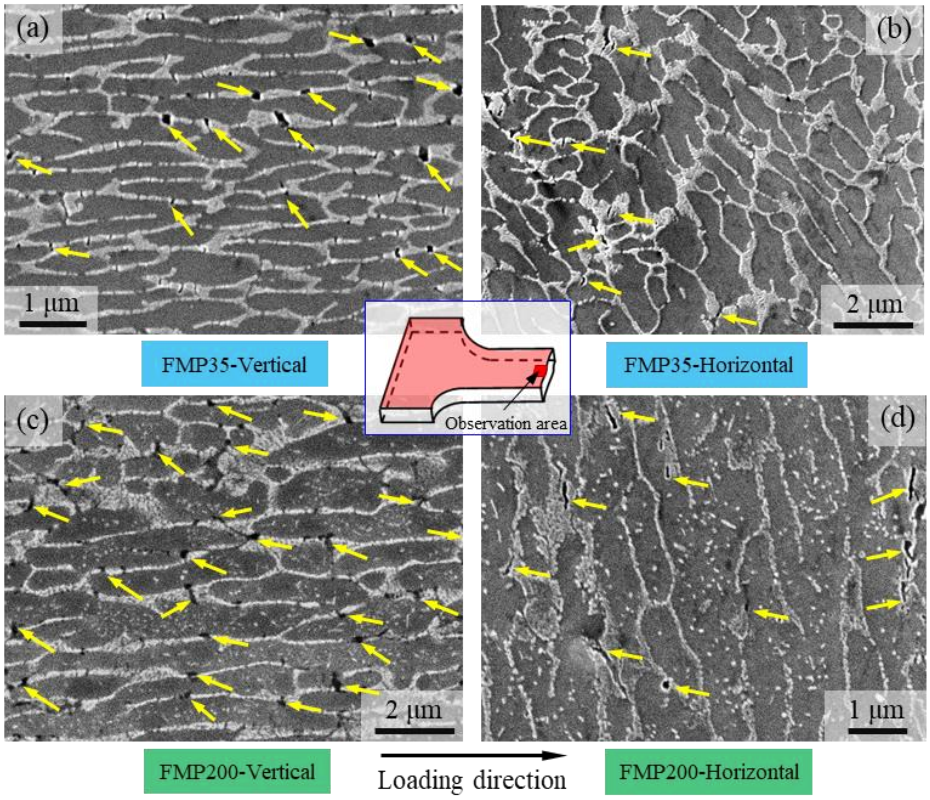

Fig. 13. Damage distribution in the FMP of the 35°C and 200°C materials along the vertical (a), (c) and horizontal (b), (d) loading directions.

In order to assess the most probable damage sites with the simulation results, the distributions of the elements in which the maximum principal stress (MPS) is higher than a threshold value are provided in Fig. 14 and Fig. 15 for the FMP 35 and FMP 200 models, respectively. Note that the effective fracture stress of the Si-rich network is unknown, thus three threshold values are selected, i.e. 2.3 GPa, 2.5 GPa and 2.7 GPa. Three common trends can be found for the two models:

- As expected, the amount of potential damage density sites decreases with increasing threshold value;

- The vertical loading direction involves a higher amount of potential damage sites with respect to the horizontal loading direction, in accordance with the higher average Si phase stress observed in Figs. 8, 9 and 12;
- When considering the strain gradient effect, the amount of potential damage sites significantly drops under the same threshold, compared to the case without strain gradient.

This last observation indicates that although the average Si phase stress is increased by the strain gradient hardening (Fig. 10(d)), the volume fraction with high MPS is effectively reduced. In other words, the strain gradient effect is expected to significantly delay damage initiation and reduce damage density. A further examination shows that the high MPS spots of the Si-rich network do not overlap between the cases with and without strain gradient. This means that the consideration of strain gradient results in a stress redistribution rather than simply increasing or decreasing the internal stress magnitude.

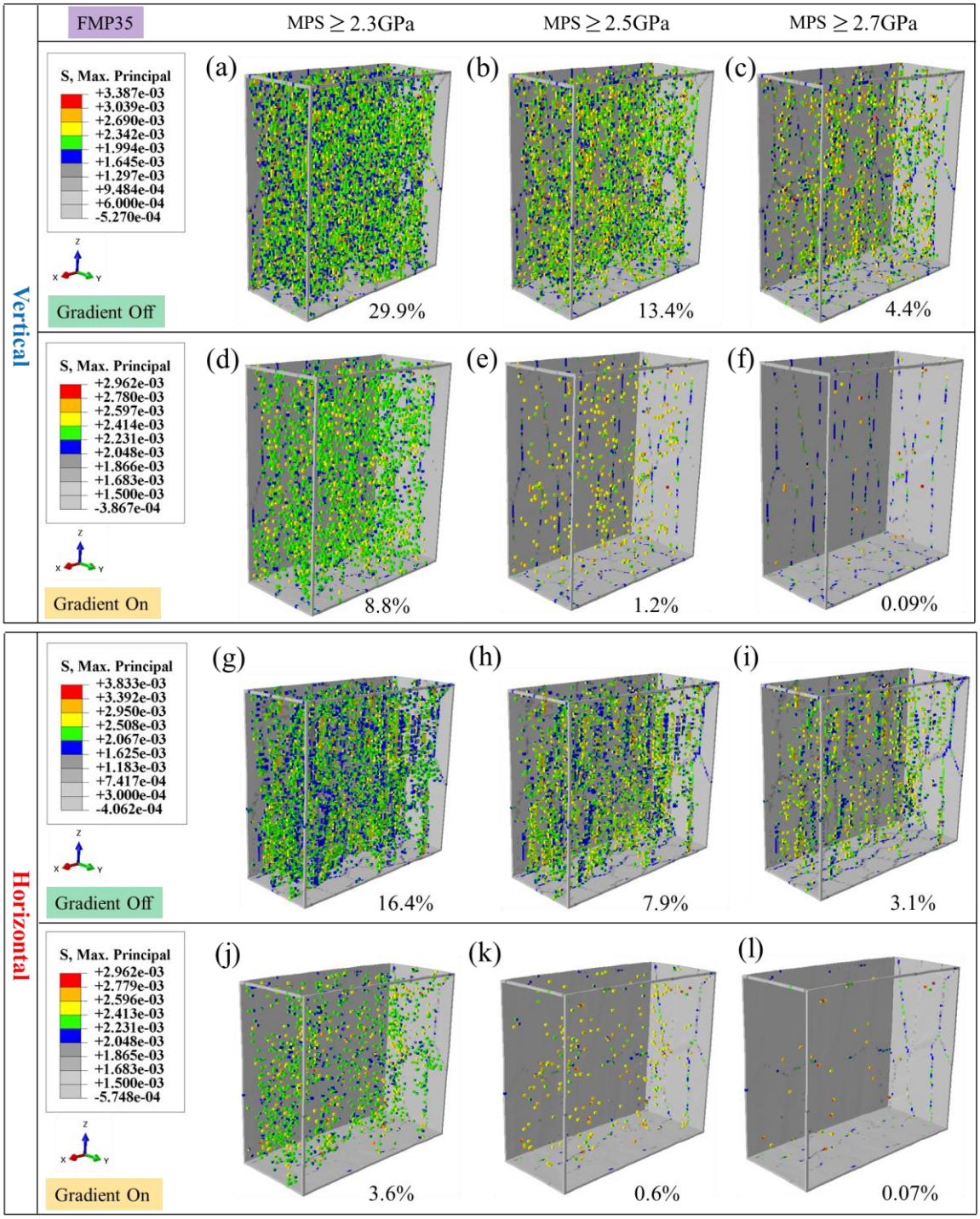

Fig. 14. Visualization of elements presenting a maximum principal stress (MPS) higher than a threshold value at the strain of 0.1 for the FMP 35. Results for the vertical direction with the CP model (a)-(c) and the MSG-CP model (d)-(f), results for the horizontal direction with the CP model (g)-(i) and the MSG-CP

model (j)-(l). The stress unit is 10^6 MPa. The percentage indicated at the bottom of each figure refers to the volume fraction of the visualized elements over all the elements representing the Si-rich network.

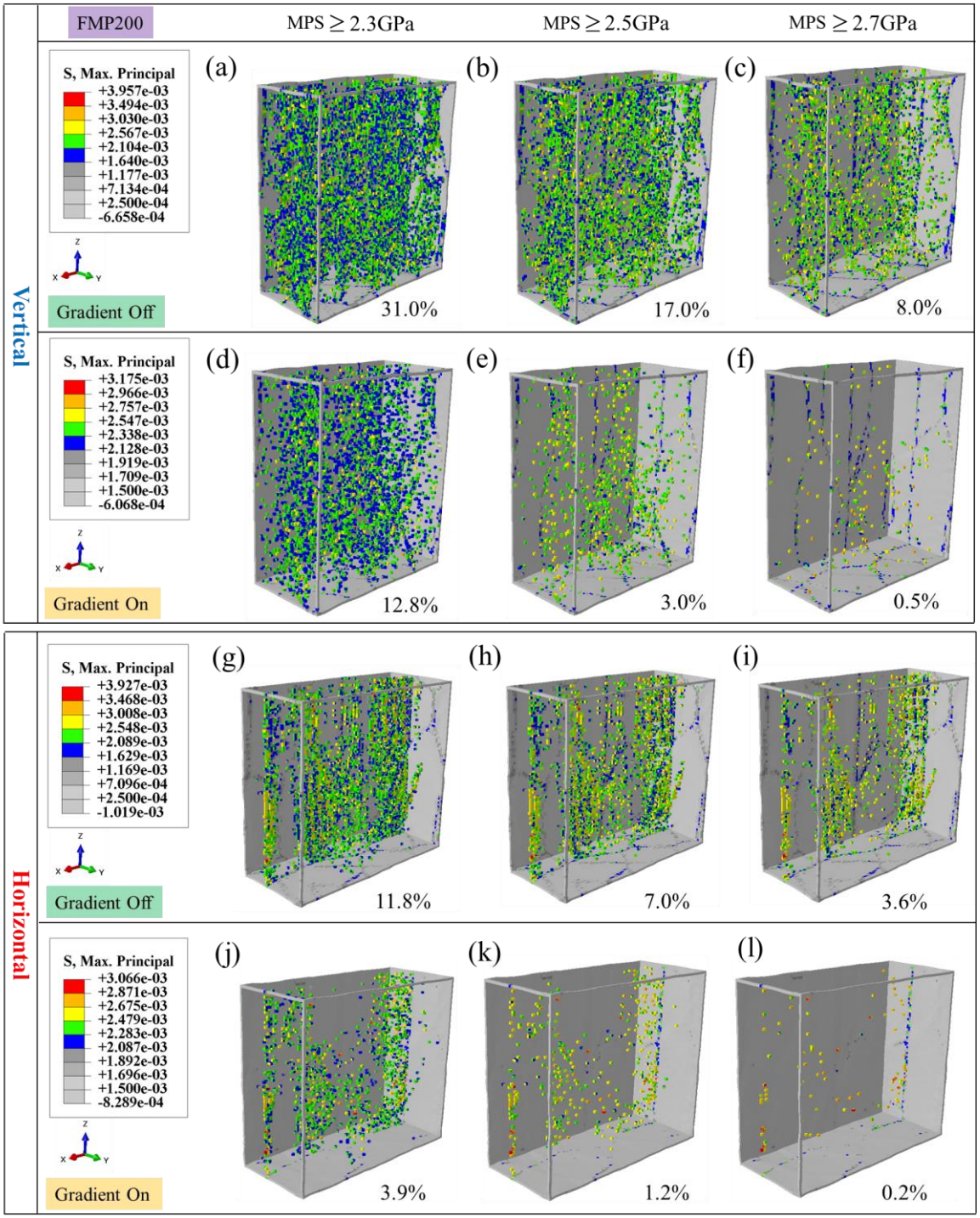

Fig. 15. Visualization of elements presenting the MPS higher than a threshold value at the strain of 0.1 for the FMP 200. Results for the vertical direction with the CP model (a)-(c) and the MSG-CP model (d)-(f),

results for the horizontal direction with the CP model (g)-(i) and the MSG-CP model (j)-(l). The stress unit is 10^6 MPa. The percentage indicated at the bottom of each figure refers to the volume fraction of the visualized elements over all the elements representing the Si-rich network.

Two differences between the FMP 35 and FMP 200 models should also be pointed out, particularly visible in the presence of the strain gradient effect: first, the FMP 200 model incorporates a higher amount of potential damage sites when comparing the results under the same loading direction and MPS threshold value; second, the FMP 200 model involves a much larger difference in the amount of potential damage sites between the two loading directions. This is more clearly reflected by Fig. 16 showing the evolution of the volume fraction of the critical Si phase (i.e. potential damage sites) for a given MPS threshold at 2.5GPa plotted as a function of engineering strain. The much steeper increase in the vertical direction of the FMP 200 model indicates a much earlier damage initiation and consequently a more significant anisotropy in damage behavior for the 200°C material. Such behaviors predicted by the simulations are in very good agreement with our former experimental observations [24] and the damage density shown in Fig. 13. It is noteworthy that results obtained with the CP model exhibit the same trends as revealed in Fig. 16, see Fig. S2 of the supplementary material.

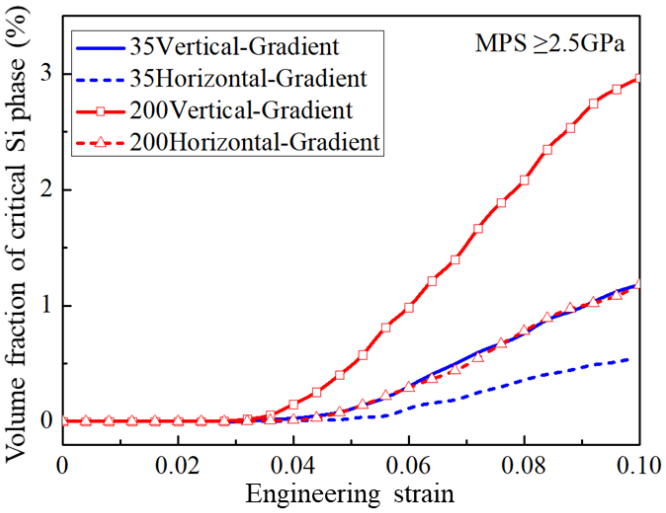

Fig. 16. Evolution of the volume fraction of critical Si phase submitted to a MPS larger than 2.5GPa. The results are obtained from the simulations with the MSG-CP model.

In summary, the damage evolution behavior and its anisotropic feature have been investigated in this section through the analysis of volume fraction of the Si-rich network presenting high MPS. The results show that the strain gradient effect can delay the damage nucleation. Moreover, the amount of potential damage sites appears to be higher under the vertical loading direction due to the higher Si phase stress, especially when the Al matrix is softer which leads to a more marked anisotropy in damage behavior. These trends are consistent with the experimental findings (i.e. higher damage density along the vertical direction for both materials and much earlier damage initiation along the vertical direction for the 200°C material) and will lay a good foundation for the further investigation on damage and fracture behavior of LPBF AlSi10Mg.

4. Conclusions

The present work investigated the mechanisms leading to the mechanical anisotropy of laser powder bed fusion AlSi10Mg, using the traditional crystal plasticity (CP) and mechanism-

based strain gradient crystal plasticity (MSG-CP) models. Two sets of RVEs were constructed to represent the Al-Si cellular structures induced by different build platform temperature (35℃ and 200℃). The influences of Al matrix strength and strain gradient on the phase stress partition were studied to understand their correlation to strength anisotropy. Moreover, the amount of possible damage sites and their densities were assessed with the maximum principal stress distribution inside the Si-rich network, based on which the origin of anisotropy in damage behavior was discussed. The main conclusions are as follows:

1. The elongated Si-rich network is confirmed to be the microscopic origin of the strength anisotropy. Nevertheless, the strength of the Al matrix significantly affects the phase stress partition and consequently the anisotropic global flow stress. The anisotropy degree, evaluated with $\sigma_{\text{global}}^{\text{V}} / \sigma_{\text{global}}^{\text{H}}$, is shown to decrease (from 1.12 to 1.03, Fig. 6) with the increase in Al matrix strength (comparison between the 200℃ and 35℃ materials) in both the experiments and simulations.
2. Strain gradient effects can effectively enhance the flow stress of both the Al and Si phases and alleviate the strength anisotropy. The enhancement and alleviation appear to be more significant for the case with intrinsically softer Al matrix (200℃ material). In future studies, strain gradient effect should be considered when calibrating CP model parameters.
3. The damage density tends to be higher under the vertical loading direction due to higher Si phase stress. The difference is more significant when the Al matrix is softer, leading to a more clear anisotropy in damage behavior for the 200℃ material. Moreover, the presence

of strain gradient tends to delay the damage by reducing the amount of high stress spots (for example, from 17% to 3% for the MPS threshold of 2.5 GPa at a strain level of 0.1).

The present work has deciphered the underlying mechanisms and the influencing factors for the anisotropy in mechanical behavior of LPBF AlSi10Mg. From the main findings stated above, it can be anticipated that a lower-aspect-ratio Si-rich network or a higher-strength Al matrix can significantly mitigate the anisotropy in both strength and ductility. This extended viewpoint lights up the way to microstructure tailoring for developing high-performance LPBF Al alloys. Moreover, the modeling strategy proposed in the present work can be extended to other materials exhibiting cellular structure, which is common to additively manufactured metallic alloys [15].

Acknowledgements

L.Z. acknowledges the support from the National Natural Science Foundation of China (No. 12272143) and the Fundamental Research Funds for the Central Universities, China (2021XXJS116). A.S. thanks the WALInnov LongLifeAM project (convention n◦1810016) funded by the Service public de Wallonie Économie Emploi Recherche (SPW-EER) and the European Research Council (ERC) for the Starting Grant ALUFIX project (grant agreement n◦716678). Dr. Douillard from Mateis, INSA Lyon is acknowledged for his help in performing the EBSD measurements.

Data availability

The data that support the findings of this study are available from the corresponding author upon reasonable request.

References

[1] A. Paolini, S. Kollmannsberger, E. Rank, Additive manufacturing in construction: A review on processes, applications, and digital planning methods, Additive Manufacturing 30 (2019) 100894.
[2] J. Plocher, A. Panesar, Review on design and structural optimisation in additive manufacturing: Towards next-generation lightweight structures, Materials & Design 183 (2019) 108164.
[3] M. Bhuvanesh Kumar, P. Sathiya, Methods and materials for additive manufacturing: A critical review on advancements and challenges, Thin-Walled Structures 159 (2021) 107228.
[4] S. Dai, Z.C. Deng, Y.J. Yu, K.Y. Zhu, Microstructure and constitutive model for flow behavior of AlSi10Mg by selective laser melting, Materials Science and Engineering: A 814 (2021) 141157.
[5] D.D. Gu, W. Meiners, K. Wissenbach, R. Poprawe, Laser additive manufacturing of metallic components: materials, processes and mechanisms, International Materials Reviews 57 (2012) 133-164.
[6] H.R. Kotadia, G. Gibbons, A. Das, P.D. Howes, A review of laser powder bed fusion additive manufacturing of aluminium alloys: Microstructure and properties, Additive Manufacturing 46 (2021) 102155.
[7] L. Zhao, L. Song, J.G. Santos Macías, Y. Zhu, M. Huang, A. Simar, Z. Li, Review on the correlation between microstructure and mechanical performance for laser powder bed fusion AlSi10Mg, Additive Manufacturing 56 (2022) 102914.
[8] N.T. Aboulkhair, M. Simonelli, L. Parry, I. Ashcroft, C. Tuck, R. Hague, 3D printing of aluminium alloys: Additive manufacturing of aluminium alloys using selective laser melting, Progress in Materials Science 106 (2019) 100578.
[9] E. Georgantzia, M. Gkantou, G.S. Kamaris, Aluminium alloys as structural material: A review of research, Engineering Structures 227 (2021) 111372.
[10] I.M. Kusoglu, B. Gokce, S. Barcikowski, Research trends in laser powder bed fusion of Al alloys within the last decade, Additive Manufacturing 36 (2020) 101489.
[11] P. Van Cauwenbergh, V. Samaee, L. Thijs, J. Nejezchlebova, P. Sedlak, A. Ivekovic, D. Schryvers, B. Van Hooreweder, K. Vanmeensel, Unravelling the multi-scale structure-property relationship of laser powder bed fusion processed and heat-treated AlSi10Mg, Scientific Reports 11 (2021) 6423.
[12] N.T. Aboulkhair, I. Maskery, C. Tuck, I. Ashcroft, N.M. Everitt, The microstructure and mechanical properties of selectively laser melted AlSi10Mg: The effect of a conventional T6-like heat treatment, Materials Science and Engineering: A 667 (2016) 139-146.
[13] L. Girelli, M. Tocci, M. Gelfi, A. Pola, Study of heat treatment parameters for additively manufactured AlSi10Mg in comparison with corresponding cast alloy, Materials Science and Engineering: A 739 (2019) 317-328.
[14] A.H. Maamoun, M. Elbestawi, G.K. Dosbaeva, S.C. Veldhuis, Thermal post-processing of AlSi10Mg parts produced by selective laser melting using recycled powder, Additive Manufacturing 21 (2018) 234-247.

[15] K.G. Prashanth, J. Eckert, Formation of metastable cellular microstructures in selective laser melted alloys, Journal of Alloys and Compounds 707 (2017) 27-34.
[16] S.A. Khairallah, A.A. Martin, J.R.I. Lee, G. Guss, N.P. Calta, J.A. Hammons, M.H. Nielsen, K. Chaput, E. Schwalbach, M.N. Shah, M.G. Chapman, T.M. Willey, A.M. Rubenchik, A.T. Anderson, Y.M. Wang, M.J. Matthews, W.E. King, Controlling interdependent meso-nanosecond dynamics and defect generation in metal 3D printing, Science 368 (2020) 660-665.
[17] W. Lefebvre, G. Rose, P. Delroisse, E. Baustert, F. Cuvilly, A. Simar, Nanoscale periodic gradients generated by laser powder bed fusion of an AlSi10Mg alloy, Materials & Design 197 (2021) 109264.
[18] L. Zhao, J.G. Santos Macías, L. Ding, H. Idrissi, A. Simar, Damage mechanisms in selective laser melted AlSi10Mg under as built and different post-treatment conditions, Materials Science and Engineering: A 764 (2019) 138210.
[19] J.G. Santos Macías, T. Douillard, L. Zhao, E. Maire, G. Pyka, A. Simar, Influence on microstructure, strength and ductility of build platform temperature during laser powder bed fusion of AlSi10Mg, Acta Materialia 201 (2020) 231-243.
[20] E. Brandl, U. Heckenberger, V. Holzinger, D. Buchbinder, Additive manufactured AlSi10Mg samples using selective laser melting (SLM): Microstructure, high cycle fatigue, and fracture behavior, Materials & Design 34 (2012) 159-169.
[21] L. Thijs, K. Kempen, J.P. Kruth, J. Van Humbeeck, Fine-structured aluminium products with controllable texture by selective laser melting of pre-alloyed AlSi10Mg powder, Acta Materialia 61 (2013) 1809-1819.
[22] X. Liu, C. Zhao, X. Zhou, Z. Shen, W. Liu, Microstructure of selective laser melted AlSi10Mg alloy, Materials & Design 168 (2019) 107677.
[23] J. Delahaye, J.T Tchuindjang, J. Lecomte-Beckers, O. Rigo, A.M. Habraken, A. Mertens, Influence of Si precipitates on fracture mechanisms of AlSi10Mg parts processed by selective laser melting, Acta Materialia 175 (2019) 160-170.
[24] L. Song, L. Zhao, L. Ding, Y. Zhu, M. Huang, A. Simar, Z. Li, Microstructure and loading direction dependent hardening and damage behavior of laser powder bed fusion AlSi10Mg, Materials Science and Engineering: A 832 (2022) 142484.
[25] U. Patakham, A. Palasay, P. Wila, R. Tongsri, MPB characteristics and Si morphologies on mechanical properties and fracture behavior of SLM AlSi10Mg, Materials Science and Engineering: A 821 (2021) 141602.
[26] M.J. Paul, Q. Liu, J.P. Best, X.P. Li, J.J. Kruzic, U. Ramamurty, B. Gludovatz, Fracture resistance of AlSi10Mg fabricated by laser powder bed fusion, Acta Materialia 211 (2021) 116869.
[27] L.C. Araújo, A.H.G. Gabriel, E.B. da Fonseca, J.A. Avila, A.L. Jardini, R. Seno, É.S.N. Lopes, Effects of build orientation and heat treatments on the tensile and fracture toughness properties of additively manufactured AlSi10Mg, International Journal of Mechanical Sciences 213 (2022) 106868.
[28] Z.H. Xiong, S.L. Liu, S.F. Li, Y. Shi, Y.F. Yang, R.D.K. Misra, Role of melt pool boundary condition in determining the mechanical properties of selective laser melting AlSi10Mg alloy, Materials Science and Engineering: A 740 (2019) 148-156.
[29] L. Zhao, J.G. Santos Macías, T. Douillard, Z. Li, A. Simar, Unveiling damage sites and fracture path in laser powder bed fusion AlSi10Mg: Comparison between horizontal and vertical loading directions, Materials Science and Engineering: A 807 (2021) 140845.

[30] Q. Yan, B. Song, Y.S. Shi, Comparative study of performance comparison of AlSi10Mg alloy prepared by selective laser melting and casting, Journal of Materials Science & Technology 41 (2020) 199-208.
[31] S. Chen, Q. Tan, W. Gao, G. Wu, J. Fan, Z. Feng, T. Huang, A.W. Godfrey, M. Zhang, X. Huang, Effect of heat treatment on the anisotropy in mechanical properties of selective laser melted AlSi10Mg, Materials Science and Engineering: A 858 (2022) 144130.
[32] D. Buchbinder, W. Meiners, K. Wissenbach, R. Poprawe, Selective laser melting of aluminum die-cast alloy-Correlations between process parameters, solidification conditions, and resulting mechanical properties, Journal of Laser Applications 27 (2015) S29205.
[33] N. Takata, H. Kodaira, K. Sekizawa, A. Suzuki, M. Kobashi, Change in microstructure of selectively laser melted AlSi10Mg alloy with heat treatments, Materials Science and Engineering: A 704 (2017) 218-228.
[34] X. Li, D. Yi, X. Wu, J. Zhang, X. Yang, Z. Zhao, Y. Feng, J. Wang, P. Bai, B. Liu, Y. Liu, Effect of construction angles on microstructure and mechanical properties of AlSi10Mg alloy fabricated by selective laser melting, Journal of Alloys and Compounds 881 (2021) 160459.
[35] T.D. Piette, R.J. Warren, A.G. Spangenberger, E.J. Hummelt, D.A. Lados, Microstructure evolution, fatigue crack growth, and ultrasonic fatigue in as-fabricated laser powder bed and conventionally cast Al-10Si-0.4Mg: A mechanistic understanding and integrated flaw-sensitive fatigue design methods, Materials Science and Engineering: A 825 (2021) 141892.
[36] E. Padovano, C. Badini, A. Pantarelli, F. Gili, F. D'Aiuto, A comparative study of the effects of thermal treatments on AlSi10Mg produced by laser powder bed fusion, Journal of Alloys and Compounds 831 (2020) 154822.
[37] A. Hadadzadeh, C. Baxter, B.S. Amirkhiz, M. Mohammadi, Strengthening mechanisms in direct metal laser sintered AlSi10Mg: Comparison between virgin and recycled powders, Additive Manufacturing 23 (2018) 108-120.
[38] L. Hitzler, C. Janousch, J. Schanz, M. Merkel, B. Heine, F. Mack, W. Hall, A. Öchsner, Direction and location dependency of selective laser melted AlSi10Mg specimens, Journal of Materials Processing Technology 243 (2017) 48-61.
[39] Y. Ou, Q. Zhang, Y. Wei, Y. Hu, S. Sui, J. Chen, X. Wang, W. Li, Evolution of heterogeneous microstructure and its effects on tensile properties of selective laser melted AlSi10Mg alloy, JMEPEG 30 (2021) 4341-4355.
[40] K. Kempen, L. Thijs, J. Van Humbeeck, J. P. Kruth, Mechanical properties of AlSi10Mg produced by selective laser melting, Physics Procedia 39 (2012) 439-446.
[41] C.G. Wang, J.X. Zhu, G.W. Wang, Y. Qin, M.Y. Sun, J.L. Yang, X.F. Shen, S.K. Huang, Effect of building orientation and heat treatment on the anisotropic tensile properties of AlSi10Mg fabricated by selective laser melting, Journal of Alloys and Compounds 895 (2022) 162665.
[42] S. Romano, A. Brückner-Foit, A. Brandão, J. Gumpinger, T. Ghidini, S. Beretta, Fatigue properties of AlSi10Mg obtained by additive manufacturing: Defect-based modelling and prediction of fatigue strength, Engineering Fracture Mechanics 187 (2018) 165-189.
[43] X.X. Zhang, H. Andrä, Crystal plasticity simulation of the macroscale and microscale stress-strain relations of additively manufactured AlSi10Mg alloy, Computational Materials Science 200 (2021) 110832.
[44] P. Li, Y. Kim, A.C. Bobel, L.G. Hector Jr, A.K. Sachdev, S. Kumar, A.F. Bower, Microstructural origin of the anisotropic flow stress of laser powder bed fused AlSi10Mg, Acta Materialia 220 (2021) 117346.

[45] D.K. Kim, W. Woo, J.H. Hwang, K. An, S.H. Choi, Stress partitioning behavior of an AlSi10Mg alloy produced by selective laser melting during tensile deformation using in situ neutron diffraction, Journal of Alloys and Compounds 686 (2016) 281-286.
[46] X.X. Zhang, A. Lutz, H. Andrä, M. Lahres, W. M. Gan, E. Maawad, C. Emmelmann, Evolution of microscopic strains, stresses, and dislocation density during in-situ tensile loading of additively manufactured AlSi10Mg alloy, International Journal of Plasticity 139 (2021) 102946.
[47] G. Vastola, G. Zhang, Q.X. Pei, Y.-W. Zhang, Controlling of residual stress in additive manufacturing of Ti6Al4V by finite element modeling, Additive Manufacturing 12 (2016) 231-239.
[48] M. Galati, L. Iuliano, A literature review of powder-based electron beam melting focusing on numerical simulations, Additive Manufacturing 19 (2018) 1-20.
[49] X.X. Zhang, D. Knoop, H. Andrä, S. Harjo, T. Kawasaki, A. Lutz, M. Lahres, Multiscale constitutive modeling of additively manufactured Al-Si-Mg alloys based on measured phase stresses and dislocation density, International Journal of Plasticity 140 (2021) 102972.
[50] M. Pinz, J.T. Benzing, A. Pilchak, S. Ghosh, A microstructure-based porous crystal plasticity FE model for additively manufactured Ti-6Al-4V alloys, International Journal of Plasticity 153 (2022) 103254.
[51] P.W. Liu, Z. Wang, Y.H. Xiao, R.A. Lebensohn, Y.C. Liu, M.F. Horstemeyer, X.Y. Cui, L. Chen, Integration of phase-field model and crystal plasticity for the prediction of process-structure-property relation of additively manufactured metallic materials, International Journal of Plasticity 128 (2020) 102670.
[52] S. Ghorbanpour, M.E. Alam, N.C. Ferreri, A. Kumar, B.A. McWilliams, S.C. Vogel, J. Bicknell, I.J. Beyerlein, M. Knezevic, Experimental characterization and crystal plasticity modeling of anisotropy, tension-compression asymmetry, and texture evolution of additively manufactured Inconel 718 at room and elevated temperatures, International Journal of Plasticity 128 (2020) 63-79.
[53] S.A.H. Motaman, C. Haase, The microstructural effects on the mechanical response of polycrystals: A comparative experimental-numerical study on conventionally and additively manufactured metallic materials, International Journal of Plasticity 140 (2021) 102941.
[54] D.K. Kim, J.H. Hwang, E.Y. Kim, Y.U. Heo, W. Woo, S.H. Choi, Evaluation of the stress-strain relationship of constituent phases in AlSi10Mg alloy produced by selective laser melting using crystal plasticity FEM, Journal of Alloys and Compounds 714 (2017) 687-697.
[55] R. Jain, M. Yadava, N. Nayan, N.P. Gurao, Combinatorial synchrotron diffraction-constitutive modelling-crystal plasticity simulation framework for direct metal laser sintered AlSi10Mg alloy, Materialia 22 (2022) 101395.
[56] Z. Li, Z. Li, Z. Tan, D. Xiong, Q. Guo, Stress relaxation and the cellular structure-dependence of plastic deformation in additively manufactured AlSi10Mg alloys, International Journal of Plasticity 127 (2020) 102640.
[57] A. Simar, K.L. Nielsen, B. de Meester, V. Tvergaard, T. Pardoen, Micro-mechanical modelling of ductile failure in 6005A aluminium using a physics based strain hardening law including stage IV, Engineering Fracture Mechanics 13 (2010) 2491-2503.
[58] Y. Huang, A user-material subroutine incroporating single crystal plasticity in the ABAQUS finite element program, Harvard Univ (1991).
[59] C.S. Han, H.J. Gao, Y.G. Huang, W.D. Nix, Mechanism-based strain gradient crystal plasticity - I. Theory, Journal of the Mechanics and Physics of Solids 53 (2005) 1188-1203.

[60] J. Liu, S. Yuan, Z. Li, M. Huang, L. Zhao, Y. Zhu, Size-dependent microvoid growth in heterogeneous polycrystals, International Journal of Plasticity 158 (2022) 103410.
[61] R. Hill, J.R. Rice, Constitutive analysis of elastic-plastic crystals at arbitrary strain, Journal of the Mechanics and Physics of Solids 20 (1972) 401-413.
[62] J.R. Rice, Inelastic constitutive relations for solids: An internal-variable theory and its application to metal plasticity, Journal of the Mechanics and Physics of Solids 19 (1971) 433-455.
[63] R.J. Asaro, J.R. Rice, Strain localization in ductile single crystals, Journal of the Mechanics and Physics of Solids 25 (1977) 309-338.
[64] G.I. Taylor, The mechanism of plastic deformation of crystals. Part I. Theoretical, Proceedings of the Royal Society of London A 145 (1934) 362-387.
[65] D. Zhou, X. Zhang, H. Wang, Y. Li, B. Sun, D. Zhang, Influence of Mg on tensile deformation behavior of high Mg-content Al-Mg alloys, International Journal of Plasticity 157 (2022) 103405.
[66] S. Gupta, V. Taupin, C. Fressengeas, J. Chevy, Crystal plasticity modeling of the effects of crystal orientation and grain-to-grain interactions on DSA-induced strain localization in Al–Li alloys, Materialia 8 (2019) 100467.
[67] O.R. Myhr, O. Grong, H.G. Fjaer, C.D. Marioara, Modelling of the microstructure and strength evolution in Al-Mg-Si alloys during multistage thermal processing, Acta Materialia 52(17) (2004) 4997-5008.
[68] V. Romanova, R. Balokhonov, A method of step-by-step packing and its application in generating 3D microstructures of polycrystalline and composite materials, Engineering with Computers 37 (2021) 241-250.
[69] T. Maconachie, M. Leary, J. Zhang, A. Medvedev, A. Sarker, D. Ruan, G. Lu, O. Faruque, M. Brandt, Effect of build orientation on the quasi-static and dynamic response of SLM AlSi10Mg, Materials Science and Engineering: A 788 (2020) 739445.